A&A 469, 459–469 (2007)
DOI: 10.1051/0004-6361:20066926

Astronomy & Astrophysics

VLT/NACO near-infrared imaging and spectroscopy of N159-5 in the LMC HII complex N159⋆,⋆⋆

G. Testor[1], J. L. Lemaire[2], L. E. Kristensen[2], D. Field[3], and S. Diana[2]

[1] LUTH, UMR 8102 du CNRS, Observatoire de Paris, 92195 Meudon, France
e-mail: gerard.testor@obspm.fr
[2] LERMA, UMR 8112 du CNRS, Observatoire de Paris, 92195 Meudon, and Université de Cergy-Pontoise, 95031 Cergy Cedex, France
e-mail: jean-louis.lemaire@obspm.fr
[3] Department of Physics and Astronomy, Århus University, 8000 Århus C, Denmark
e-mail: dfield@phys.au.dk

Received 13 December 2006 / Accepted 14 March 2007

ABSTRACT

We present high-resolution near-infrared imaging of the compact HII region N159-5 and its immediate environment in the giant-star forming region N159 in the LMC. N159-5 was observed at high spatial resolution ~0.″11−0.″25 in the *K*-band using the ESO Very Large Telescope UT4 (VLT), equipped with the NAOS adaptive optics system. Our data reveal that N159-5 has a complex morphology formed mainly by two wings and probably a single central bright star, embedded in diffuse emission of ~4.″5 diameter. A remarkable embedded tight cluster of approximatively the same size, containing at least 38 faint stars coinciding with N159-5, is also detected. Such clusters can be found in galactic HII regions like the star-forming regions SH2 269 or M42. At the location of the radio peak, especially in the bright western wing, this cluster is rich in stars. Spectroscopic observations reveal that the diffuse region is constituted mainly of dust continuum and that the bright star #2-55 could be of type O8 V. A comparison with the radio observation flux of N159-5 published in the literature seems to show that the bright star #2-55 is not the only ionization source of N159-5. Towards N159-5 molecular H_2 emission is detected. A model of the region is proposed.

Key words. galaxies: Magellanic Clouds – ISM: individual objects: N159-5 – stars: formation

1. Introduction

The Large Magellanic Cloud (LMC) is rich in HII regions and young OB associations. Because of its known and relatively small distance (50 kpc) (Storm et al. 2004) and face-on position relatively free from foreground extinction, it is well suited for the study of both individual stars and very compact objects, as well as global structures. The LMC is also an ideal laboratory for investigating the formation and evolution of massive stars in a low-metallicity environment.

Massive stars play a major role in the dynamical evolution of galaxies. They are responsible for the ionization of the interstellar medium while the associated stellar winds and supernovae are dominant sources of mechanical energy. They are also a main driver of chemical evolution in the universe at the end of their lives. Some understanding of the early stages of massive star formation in our galaxy is emerging. However, this is not the case in external galaxies of low-metallicity environment such as the Magellanic Clouds (MCs). There are two main reasons for this dearth of information: one is the lack of the high–spatial-resolution data at a distance of 50−65 kpc, necessary to disentangle the individual massive stars from their surrounding environment; and the other is the strong reddening, typical of young, massive-star regions.

Some progress has been made following the discovery of compact HII regions in the MCs, now generically named HEBs (High Excitation Blobs) (Heydari-Malayeri & Testor 1982). HEBs are characterized by small size, high density, extinction, and excitation. The line ratio [OIII]$\lambda\lambda$4959+5007/Hβ used as excitation parameter ranges typically between ~7−10. They are probably excited by more than one newborn massive star arriving on the zero-age main sequence (Walborn & Parker 1992). With a diameter of 0.5−2 pc they are at the frontier of compact HII (CHII) and HII regions. HEBs represent the early evolutionary stages of recent star formation (Churchwell 1992) and are important in the context of massive-star formation under low metallicity.

So far, only eight HEBs have been found in the MCs and they are listed in Testor (2001). Optical HST observations of some of them have revealed tight star clusters and complex structures (0.03 pc) and are listed in Meynadier et al. (2004). Nevertheless, due to the reddening, little is known about their exciting sources. In the present paper we focus on the HEB N159-5 (Heydari-Malayeri & Testor 1982), a compact HII region of size ~6″ (1.5 pc) in the HII region N159 (Henize 1956) coinciding with the IRAS source 05405-6946. This compact HII region features high excitation [OIII](5007+4959)/Hβ ~ 8 and is affected by the highest extinction of A_V ~ 5 mag (Heydari-Malayeri & Testor 1985) and 4.5−6.7 mag (Israel & Korneef 1991) among the HEBs. South of 30 Doradus at a distance of ~600 pc there is a chain of Henize giant HII regions, namely N158, N160 and N159. It is believed that the star formation

⋆ Based on observations obtained at the European Southern Observatories, El Paranal, Chile.
⋆⋆ Table 3 is only available in electronic form at http://www.aanda.org

process started in 30 Doradus, and N159, the most southerly region, corresponds to the still quiescent part of the 30 Doradus complex (Israel et al. 1996). The first extragalactic Young Stellar Object (YSO) labelled P1 was discovered by Gatley et al. (1981) in N159. The region also contains the first extragalactic type I OH maser (Caswell & Haynes 1981) and a H_2O maser (Scalise & Braz 1981). Later a second YSO, labelled P2, was discovered by Jones et al. (1986) in N159A.

N159 is associated with the most important concentration of molecular gas in the LMC (Jones et al. 1986; Brooks & Whiteoak 1997; Johansson et al. 1998). This molecular emission is composed of three distinct giant molecular clouds (GMCs), known as N159E, N159W and N159S. The HEB N159-5 is associated with the GMC N159E (Bolatto et al. 2000) and has also been observed in ^{12}CO 3–2 by Fukui (2005). In N159E the dust mass is particularly high (Rantakyrö et al. 2005). A 5 GHz radio continuum map of N159 with a spatial resolution of about 5″ (Hunt & Whiteoak 1994) shows continuum features numbered #1 to #5 where #1 is associated with N159-5. Using the Infrared Space Observatory Camera (ISOCAM) with a spatial resolution of 3″, Comeron & Claes (1998) obtained an image of N159-5 labelled LI-LMC 1501E at 15 μ. N159-5 has been observed at 3 and 6 cm by Indebetouw et al. (2004) using the Australia Telescope Compact Array (ATCA). They obtained radio continuum maps at a resolution of 3″ and found a radio source superposing the western part of N159-5. This source has also been observed by Jones et al. (2005) with a resolution of ∼2″ using Spitzer IRAC bands (3.5, 4.5, 5.7 and 7.9 μm). Their observations show that N159-5 is one of the brightest regions in N159. In Martin-Hernandez et al. (2005) N159-5 is assumed to be ionized by an O4 star.

Infrared photometry of N159-5 obtained by Israel & Korneef (1991) showed that the object is associated with H_2 emission and is a good candidate for a cocoon star. Using deep near-infrared imaging Nakajima et al. (2005) found that N159-5 is associated with their Herbig Ae/Be N159-Y4 cluster, which harbours embedded massive stars. These NIR data give a clear indication of ongoing star formation.

N159-5 has been observed with the HST at a resolution of 0.″1 by Heydari-Malayeri et al. (1999) using visible filters. They found that N159-5 is a butterfly-shaped ionized nebula with the wings separated by ∼2.″3 (0.6 pc). They detected features resembling a "smoke ring" and a "globule" in the western and eastern wing respectively. A detailed near-infrared *JHK* study of the stellar population associated with N159-5 using the VLT and ISAAC, is presented in Meynadier et al. (2004). They suggest that the central star could be a single star with an initial mass of 50 $M_\odot$ and affected by an extinction A_V of ∼7 mag.

In this paper we present VLT images and spectroscopy of N159-5 through K_s filters using adaptive optics, providing high-spatial-resolution images. Section 2 describes the observations and data reduction and presents the K_s photometry towards the N159-5 region. In Sect. 3 we examine the morphology of N159-5, its stellar population and ionizing source. This section also includes a comparison with the galactic HII region SH2 269, as well as a description of the NIR and radio continuum and the H_2 emission. Finally we propose a model for the N159-5 region. In Sect. 4. the results are summarized.

2. Observations and data reduction

NIR observations of N159-5 were obtained at the ESO-VLT during October and December 2004. Images and spectra were obtained using NACO composed of the Nasmyth Adaptative Optics System (NAOS) and the High Resolution IR Camera and Spectrometer (CONICA). The detector was a 1024 × 1024 SBRC InSb Alladin 3 array. For imaging we used the camera mode S54 and S27. The field of view of the S54 camera was 54″ × 54″ with a pixel size of 0.05274″, corresponding to 0.013 pc at the distance modulus of 18.5 for the LMC (Cole 1998). The field of view of the S27 camera was 27.″15 × 27.″15 with a pixel size of 0.02637″, corresponding to 0.0066 pc. For spectroscopy we used the same camera in S54 mode. As an adaptive optics (AO) reference source for wavefront sensing we used the object itself (N159-5), corresponding to star #371 of $K = 14.30$ mag in Meynadier et al. (2004). The conditions were photometric and the average seeing was of 0.″8 in the visible. After subtraction of the average dark frame, each image was divided by the normalized flat field image. The data were reduced with the ESO software packages MIDAS and ECLIPSE.

Table 1. Log of photometric VLT/NACO observations.

Id.	Filter	Expo. $t(s) \times n$	Mode	Date	Seeing (″)
N159-5	K_s	20×20	S54	8/10/2004	0.6–0.9
	K_s	60×11	S27	4/12/2004	0.6–0.9

Table 2. Log of VLT/NACO long-slit spectroscopic observations.

Id.	Date	Slit	Exposures $t(s) \times n$	Mode	$\lambda/\delta\lambda$	Seeing (″)
(a)	10/10/2004	172 mas	200×20	S54-4-SHK	500	0.6–0.9

2.1. Imaging

Images were obtained through the K_s filter (Table 1). The autoJitter mode was used: that is, at each exposure, the telescope moves according to a random pattern in a 6″ × 6″ box. The mean PSF (point-spread function) measured on several stars in the K-band was ∼0.″11 and 0.″22 for the mode S27 and S54 respectively. The PSF increases slightly at the sides of the images following the decreasing Strehl ratio as the distance from the reference star for AO increases.

2.2. Spectroscopy

Spectroscopy was performed in the mode S54-4-SHK (broadband filter) giving a coverage of 1.3 to 2.60 μ, a linear dispersion of 1.94 nm/pixel and a spatial scale of 53 mas/pixel. A long-slit spectrum (a) was taken, (PA = 130.3°) crossing our stars #2-55 and #2-91 (Table 2). The slit width was 172 mas and the spectral resolution ∼500. For each exposure the detector integration time (DIT) was 200 s. Twenty exposures were obtained in the Autonod on slit mode which allows spectroscopy of moderately extended objects. In order to remove telluric absorption features, a star with a similar airmass was observed as the telluric standard. Spectroscopy was reduced with the MIDAS software package LONG.

2.3. Photometry

In Figs. 1 and 2 we present K_s-band images containing N159-5. These images, that we name Field 1 and Field 2, are extracted from the fields of view of the S54 and S27 camera respectively. The instrumental magnitudes of the stars were derived using

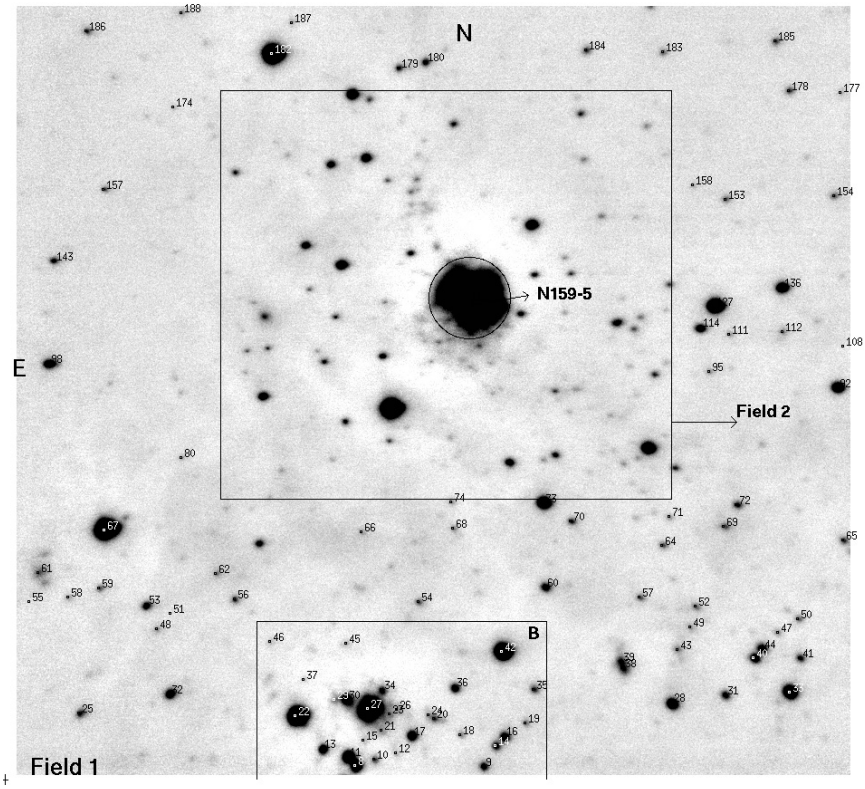

Fig. 1. Finding chart (*K*-band image) corresponding to Field 1 containing N159-5 obtained with the S54 camera. The cluster N159-5-B slightly cut to the south is outlined as well as Field 2 represented in Fig. 2. The numbering refers to Table 3a (online material). The diffuse nebular area of N159-5 is outlined by a circle of diameter ∼4.″5. The total field size corresponds to 51″ × 47″ (or 12.8 pc × 11.8 pc).

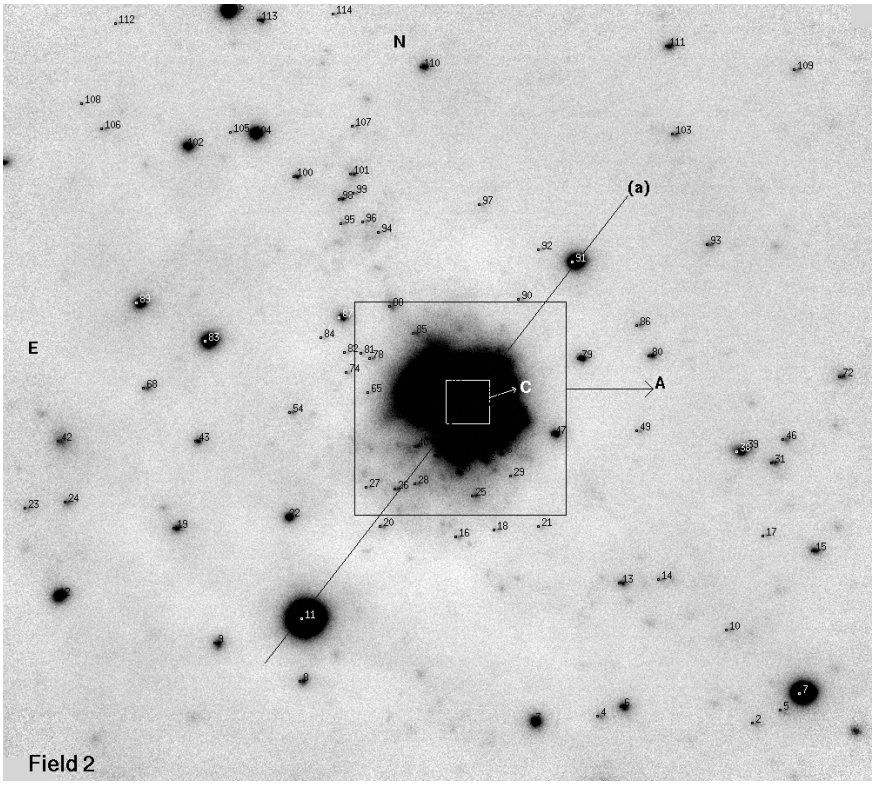

Fig. 2. Finding chart (*K*-band image) corresponding to Field 2 obtained with the S27 camera for the stars detected towards N159-5. The numbering refers to Table 3b (on line material). The inset A (6.″6 × 6.″6) containing the HEB N159-5 as well as the small inset C (1.″34 × 1.″34) containing the central star #2-55 are outlined. The location of the slit (a) used in the spectroscopic mode is indicated by a solid line. The total field size corresponds to 26.″9 × 23.″8 (or 7 pc × 6 pc).

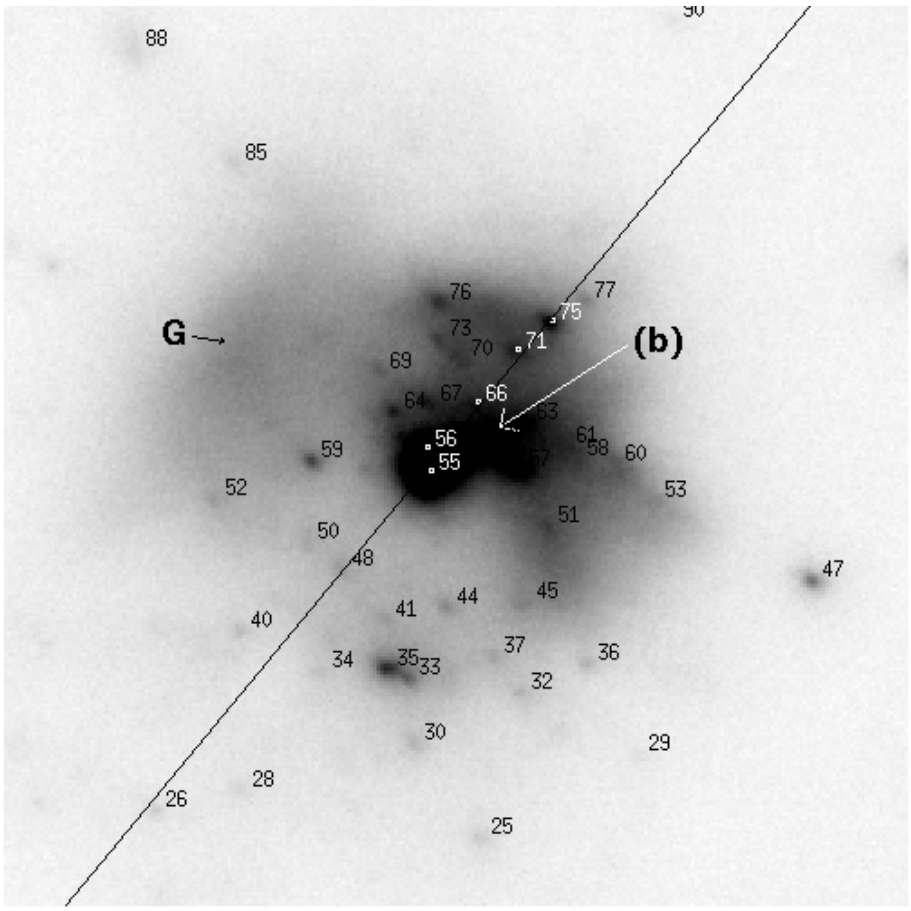

Fig. 3. Finding chart for region A in Field 2 corresponding to a field of 6.″6 × 6.″6 (or 1.63 pc × 1.63 pc) containing the cluster N159-5-A. The bright central part of the western wing (b) and the "globule" G are indicated by arrows.

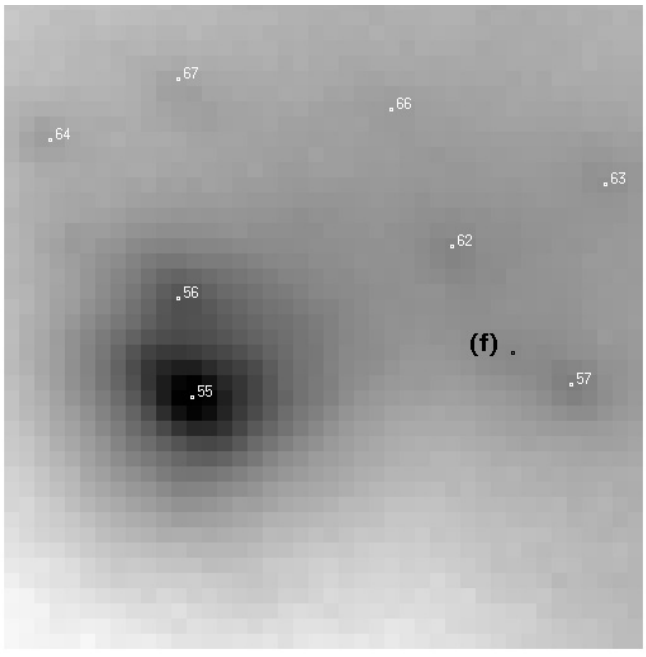

Fig. 4. Finding chart for inset C in Field 2 (logarithmic scale) corresponding to a field of 1.″34 × 1.″34 (or 0.34 pc × 0.34 pc). In this inset resolved and unresolved stars like the feature (f) of the concentration of stars towards star #2-55 are shown.

DAOPHOT/NSTAR (Stetson 1987). In order to compute the PSF we used several stars uniformly spread out in the fields, thus averaging the effect of the Strehl ratio (see Sect. 2.1). The photometric calibration was obtained using bright and isolated stars in the N159-5 field observed by Meynadier et al. (2004) with ISAAC. These stars are #199, #287 and #450 for Field 1 and #353 and #404 for Field 2. The conversion of pixel coordinates to α and δ of the two fields was obtained using the star #353. The relative positions of our stars are accurate to around 0.″1. In each field the stars are identified by a number. Several faint stars that lie below the detection level, or are slightly extended, are not detected by DAOPHOT and not identified. Due to the crowding and the large range of intensity scale in the diffuse nebula, two insets, A and C, are outlined in Fig. 2. Their enlarged finder charts (Figs. 3 and 4) allow a better view of the stars and their identifications. In Tables 3a and b (online material), the astrometry and the K_s photometry with photometric errors of Field 1 and Field 2 are given. In Col. 1, the identification of the stars begins with a number corresponding to the number of the field analysed. Only the stars outside Field 2 are listed in Table 3a. The tables show, when available, in Cols. 8 and 9, the corresponding number and magnitude found in Meynadier et al. (2004). In Fields 1 and 2 the average photometric errors of the stars detected at 3σ reported by DAOPHOT are ∼0.02 mag for stars of magnitude brighter than 17 mag. In the range of 17−20 mag the average photometric errors are less than 0.04 mag. To compare our photometry with Meynadier et al. (2004) we did not take into account their unresolved stars #317.1, #318, #457 and #517. The comparison of our star with those of Meynadier et al. (2004), in a range of 12.9−18.4 mag, gives for Table 3a and 3b, a same standard deviation of the slope of ∼0.01 mag and a rms error of ∼0.05 mag, which is in good agreement with Meynadier et al. (2004).

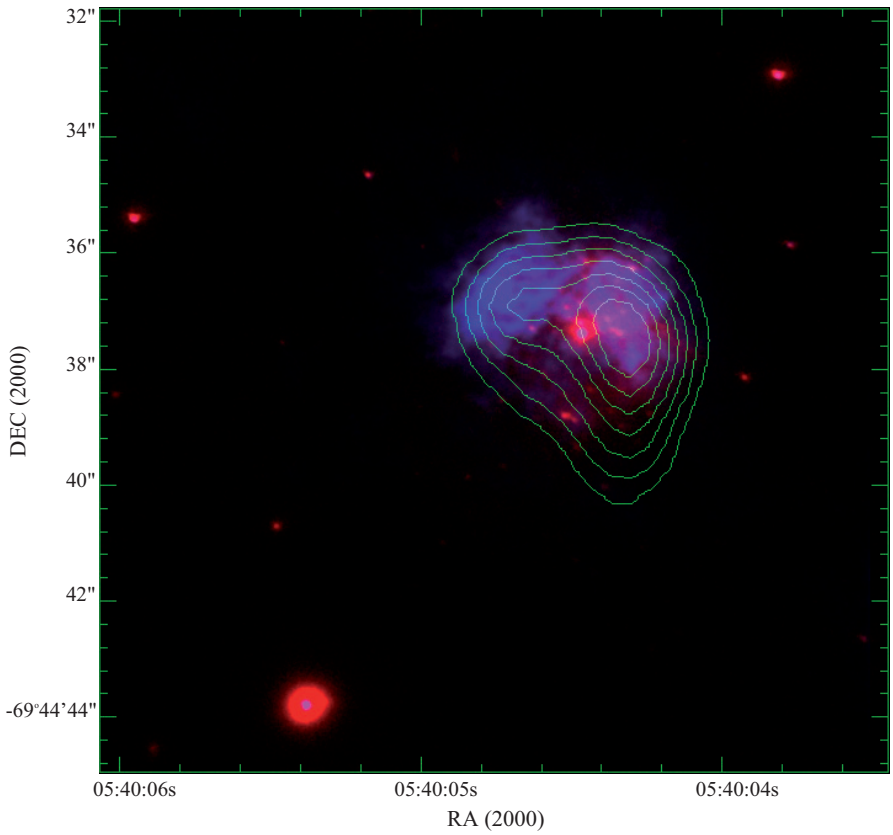

Fig. 5. Composite Hα K_s image (Hα = blue, K_s = red) overlaid with the 3 cm radio contours (Indebetouw et al. 2004). The field corresponds to 13.″2 × 13.″2 or ∼3.3 × 3.3 pc.

3. Results and discussion

3.1. General morphology

3.1.1. The HEB N159-5

Through the HST Hα filter (Heydari-Malayeri et al. 1999), N159-5 is seen to consist of two distinct ionized wings (blue component in Fig. 5) of about the same intensity in a diameter of ∼5.″Between these two wings there is a low brightness zone of ≈2″ width showing an overall shape reminiscent of a butterfly. In this zone they found a faint star that could be the major source of ionization. They also found two other faint stars in the right wing and one in the left wing outside the "globule" (Heydari-Malayeri et al. 1999).

Through the K_s filter, N159-5 appears less complex. It is composed of two wings of differing intensity (Fig. 3) embedded in a diffuse nebular region of ∼4.″5 with a very bright central star #2-55 (Fig. 4). This star of K = 14.33 mag is centered on the 2MASS point source 05400448-6944375 of K = 11.73 (Cutri et al. 2003). Figure 6 shows the plots of the intensity distribution in the Hα and K-bands in the direction of the slit (a) crossing stars #2-55 and #2-91 (Fig. 2). In this figure our bright star #2-55 coincides with the faint central star of magnitude =17.9 in Heydari-Malayeri et al. (1999). The western wing (Fig. 3) is bright and elongated in the south-west and north-east direction (1.3 × 2.″8 or 0.3 × 0.7 pc). The eastern wing is very faint and its maximum intensity coincides fairly well with the position of the "globule" (G) (Fig. 3). According to the classification of Martin-Hernandez et al. (2005), the size of N159-5 corresponds to a classical HII region rather than a compact one, the apparent compactness of the HEB N159-5 being mainly due to its distance. In addition, the K image reveals a remarquable dense, embedded stellar cluster that we label N159-5-A, coinciding approximatively with the diffuse nebular region.

3.2. The embedded cluster N159-5-A

N159-5-A lies in the cluster N159-Y4 in N159E of Nakajima et al. (2005). N159-Y4 of size ∼16 pc centered at [5 40 04.4−69 45 08 2000] is a second-generation cluster, still embedded in its natal cloud. N159-Y4 exhibits extinction and could be an embedded OB cluster. Meynadier et al. (2004) have studied a field of 32 pc × 33 pc in the *JHK*-bands, centered on N159-5. They found a young population of massive O stars fitting the three Myr isochrone and a second older population (1 to 10 Gyr) of low mass stars. Towards their star #371 observed with a spatial resolution ranging from 0.″6 to 1.″1 containing mainly our star #2-55, they found a strong mean extinction of A_V = 7 and no IR excess. In the N159-5-A cluster (Fig. 3) we detect within the K nebulosity of ∼5″ diameter at least 38 stars including star #2-55. N159-5-A appears to be composed of two stellar concentrations, one located in the western wing and the second one somewhat to the south of the two wings. The eastern wing contains only a few stars and no star is found towards G (Fig. 3). Table 4 lists the apparent K-magnitude distribution, bin 0.5 mag, of the detected stars and their identification in N159-5-A. The distribution increases towards the faintest stars up to K ∼ 17.5 mag, which is our approximate completeness limit, the magnitude at which we should have detected all stars, and then decreases slightly to K ∼ 20 mag. According to the extinction law $\delta K = 0.112 A_V = 0.78$ Rieke & Lebofsky (1985),

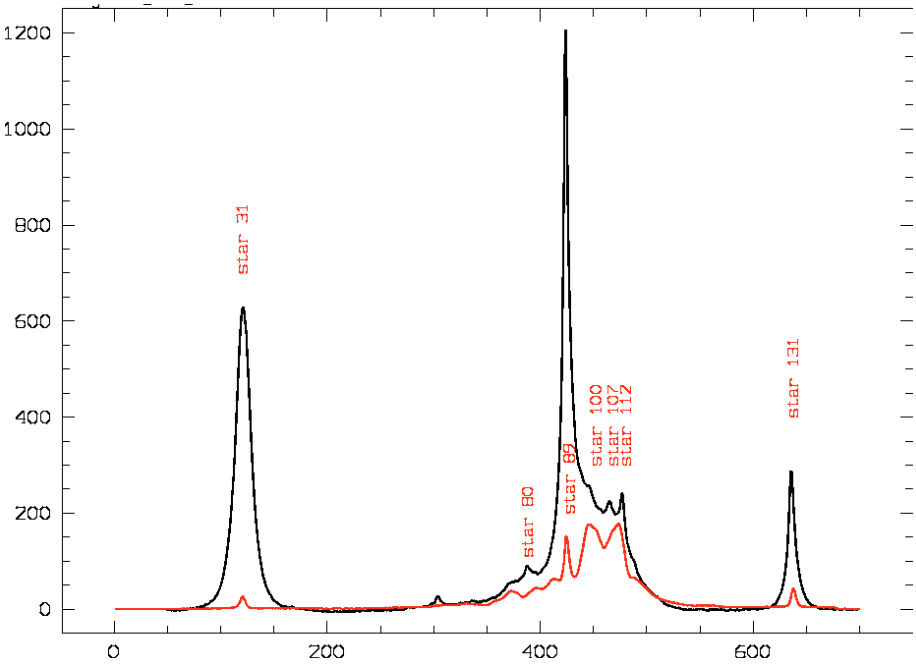

Fig. 6. Intensity distribution in the direction of the slit crossing #2-11, #2-55 and #2-91 (Fig. 1). The distribution in the K-band image is represented by a solid line and in the HST Hα-band image along the same direction by a dotted line. The intensity distribution range corresponds to 13.″9 or 3.5 pc (1 pixel = 0.″05273).

Table 4. Stars in N159-5-A.

Bin	n	Id	$M_\odot$
14–14.5	1	55	40–33
16–16.5	1	75	17–14
16.5–17	6	51, 53, 57, 56, 62, 64, 35	14–11
17–17.5	14	60, 59, 61, 63, 66, 70, 71, 73, 76, 77, 79, 33, 36, 58	11–9
			11–9
17.5–18	7	30, 44, 45, 52, 67, 69, 85	9–7
18–18.5	3	32, 40, 56	7–6
18.5–19	3	34, 41, 48	6–4.5
19–19.5	2	21, 37	4.5–3
19.5–20	1	50	3–2.5

Notes. Column 1: reddened stars, Col. 2: magnitude distribution, Col. 3: identified cluster members (Field 2), Col. 4: mass$_i$ derived after dereddening (3 Myr and Z = 0.008).

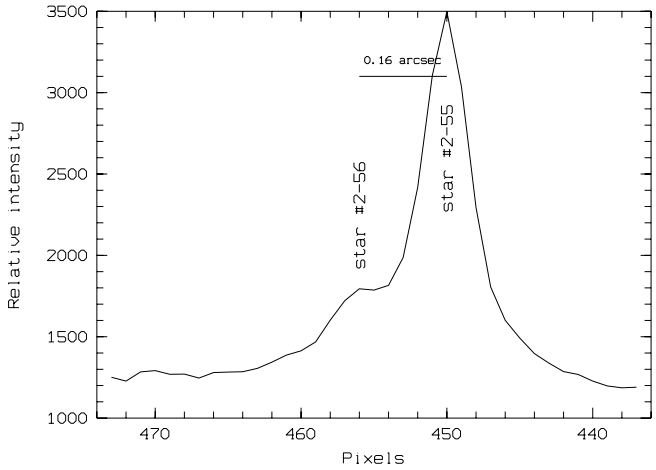

Fig. 7. Intensity distribution in the K-band over an angular range of 0.″99 in the direction of the slit passing through #2-55 and #2-56, which lie 0.″16 apart (1 pixel = 0.″02637).

and assuming a mean A_V = 7 mag for N159-5, the dereddened stars of N159-5-A range from K-magnitude 13.22 to 19.72. Due to the strong extinction and no IR excess in N159-5, most of these stars could be massive stars. If we assume an age of about three Myr suggested by Meynadier et al. (2004) for the massive stars in the N159 region, according to the Lejeune & Schaerer (2001)'s table with Z = 0.008, these stars in N159-5-A could be mainly reddened class V OB star candidates of intermediate and high mass (2.5−40.0 $M_\odot$). Masses derived on this basis are shown in Table 4. The presence of intermediate-mass group III Herbig Ae/Be stars with intrinsically red color (Nakajima et al. 2005) is not excluded, while the low-mass pre-main sequence stars of greater magnitude than our detection limit at ∼20 mag are not detectable. Inset C, from Fig. 2 and in detail in Fig. 4, shows that the bright central part (b) of the western wing (Fig. 3) contains at least five embedded stars, #2-56 #2-57, #2-62, #2-63 and #2-66, and several features such as nebular emissions or unresolved stars like feature (f) close to star #2-57. The extension of the wings of star #2-55 (Fig. 4) could be due to dust-enshrouded faint unresolved stars. The nearest resolved star to star #2-55 is the star #2-56 of K = 16.80 mag at a distance of ∼0.″16 to the north. This star is seen to be very faint and well-resolved on the HST Hα image (Heydari-Malayeri et al. 1999). Star #2-55, obtained with a spatial resolution of 0.″11 ∼ 0.03 pc, is probably a single star. This is illustrated by the intensity distribution along the direction crossing stars #2-55 and #2-56 shown in Fig. 7.

3.2.1. The cluster N159-5-B and peculiar stars

The K-band photometry of cluster B in Meynadier et al. (2004) is shown in Fig. 1, labelled N159-5-B. At least 32 stars have been found in an area of 16″ × 9″, but not all are analysed by DAOPHOT. The magnitudes and the positions of the stars in N159-5-B are found in Table 3a. The bright star #1-27 appears centered on a faint subcluster formed by at least 10 stars within a diameter of ∼4″ (Fig. 8). The reddest star labelled #317.1 found by Meynadier et al. (2004) has in fact two components, #1-38 and #1-39 of magnitude 16.81 and 16.74. Their peculiar elongated object #517 is formed by three components. The central

Table 5. Ionization in N159-5.

Source	$L/L_\odot$	log $N_{\rm Lyc}$ (s^{-1})	Sp. type	Sp. type [s]	Aperture ($''$)	λ
N159-5		49.4[mvh]	O4 V	O4 V	1–2	6 cm
		49.2[ijc]	O6 V	O5 V	1–2	3–6 cm
2-#55			O8 V		0.25	K-band spectrum

[mvh] Martin-Hernandez et al. (2005); [ijc] Indebetouw et al. (2004); [v] type derived from Smith et al. (2002).

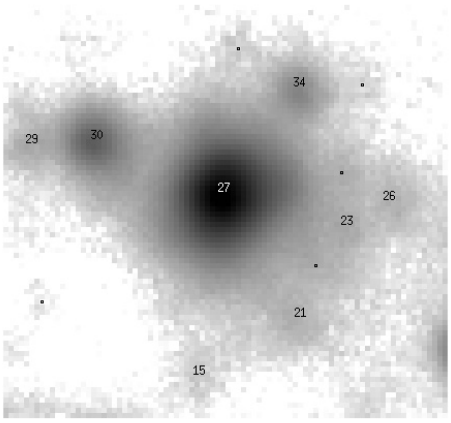

Fig. 8. Finding chart of the star concentration (logarithmic scale) around the star #1-27 in N159-5-B. The field size is $4\farcs1 \times 4\farcs1$ or 1 pc × 1 pc. The stars indicated by a dot are not analysed by DAOPHOT.

one #1-61 is analysed by DAOPHOT and the two other ones are probably slightly extended. The stars #365, #404 and #499 suggested to be complex by Meynadier et al. (2004), corresponding to our stars #1-42, #2-11 and #1-67 respectively, are probably in fact single stars. Star #2-42 and star #1-20 in cluster N159-5-B appear to be embedded in a diffuse nebulosity.

Like N159-5-A, N159-5-B lies at the edge of a molecular peak (Meynadier et al. 2004) and is rich in stars. The presence of the subcluster containing star #1-27, which is located on the upper HR diagram of Meynadier et al. (2004) near the massive star #1-42, strengthens the assumption that N159-5-B could also be a star-forming area, less extinguished because probably more evolved than N159-5-A.

3.3. The ionizing source

Martin-Hernandez et al. (2005) found a Lyman continuum flux of log $N_{\rm Lyc}$ = 49.4, and Indebetouw et al. (2003) found 49.2. Using the new spectral classification of Smith et al. (2002) we estimate, from their fluxes, the type of the ionizing source of N159-5 to range from O4 to O5 (Table 5). Our spectrum (a-3) Fig. 9, crossing stars #2-55 and #2-91 (Fig. 2) shows a ratio Brγ/He I 2.112 μ lines of ∼0.04. Such a ratio, according to Hanson et al. (2003) in their Table 3, indicates that the HII region could be ionized by a single O star of spectral type O7 V or hotter.

In the spectrum (a-3) Fig. 9 the He II 2.185 μ absorption line is not detected, if present. The detection is not possible with our signal/noise of ∼1 and low spectral resolution. The NIII 2.115 μ emission lines is also not detected. According to Bik et al. (2005) when the He II absorption line is not present the spectral type of a star should be later than O7/O8, so we classify star #2-55 to be of type O8 V. The radio spectral type of the ionizing source of the whole nebula given by Martin-Hernandez et al. (2005) and Indebetouw et al. (2003) is of type O4 and O5 respectively. The comparison with the type O8 V derived from our spectroscopy (Table 5) of the bright central star #2-55 shows that other massive stars must contribute to the ionization of N159-5. These stars could belong to the deeply embedded cluster N159-5-A and especially to the concentration of stars in the north-west wing (Fig. 3). The ratio Brγ/He I 2.112 μ lines of ∼0.035 of the integrated spectrum (a-2) in Fig. 9 strengthens the evidence for the presence of such massive stars. In N159-5 the luminosity excess in addition to the flux of the ionizing star #2-55 of type O8 V could be produced by 5 up to 9 O8 V stars, depending on the radio spectral type derived from data of Indebetouw et al. (2003) or Martin-Hernandez et al. (2005).

3.4. Comparison with the galactic region SH2 269

SH2 269 (Sharpless 1959) is an HII region of similar size, ∼1.2 pc at 2 kpc (Heydari-Malayeri et al. 1982).

SH2 269 and N159-5 share similar characteristics:

- in the optical band they are composed of a central star and two wings, in the form of a butterfly (Heydari-Malayeri et al. 1982);
- in the *NIR*-band they contain an embedded faint red cluster (Eiroa & Casali 1995);
- they feature a strong *NIR* emission and more stars in the western wing (Eiroa & Casali 1995; Jiang et al. 2003);
- they present ionization that is driven not only by the central bright star, but also by other embedded low-to high-mass stars.

A faint red cluster of ∼1 pc similar to those in N159-5-A and in SH2 269 also exists in the well known Orion region M42 (O'Dell 2001). We make a comparison with the Orion region in Sect. 3.8. The presence of some massive stars among lower mass stars in all these clusters could strengthen the proposition of Jiang et al. (2003) that these could play a role in the formation of massive stars.

3.5. The continuum emission

Figure 3 shows the diffuse emission centered on star #2-55. At the location of (b) the nebular emission is found particularly bright. This effect is probably due to the combination of the reflected dust continuum emission with the continuum of resolved and numerous unresolved stars in (b). In support of this, the intensity distribution along the slit (a), near the Brγ line shows a strong continuum/Brγ ratio of 0.30−0.6 over a range of $5\farcs8$ around star #2-55 (Fig. 10).

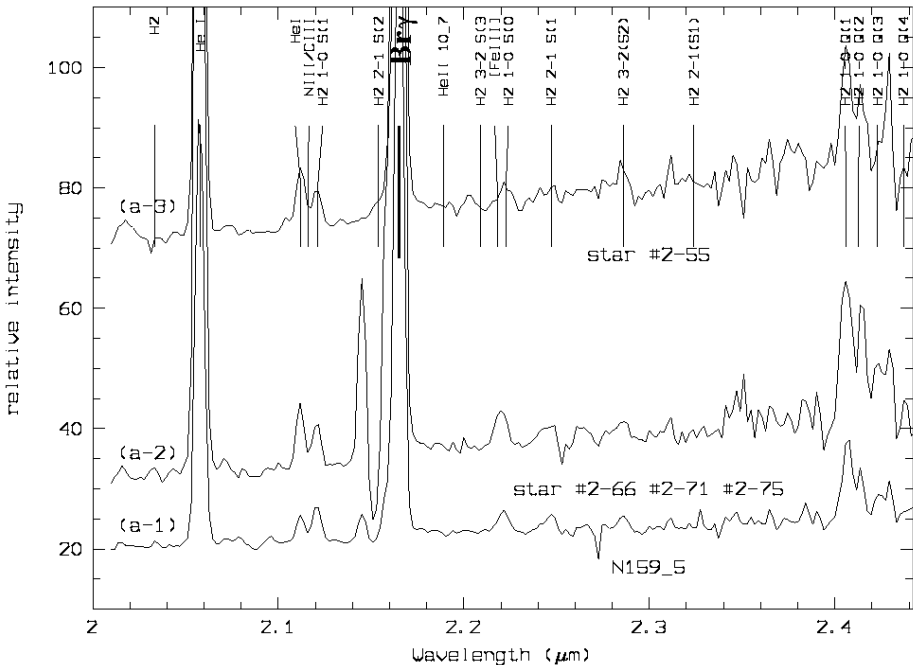

Fig. 9. Three 1D spectra extracted by summing a pixel range along the slit (a) are plotted in the range 2. μm−2.44 μm. The spectrum (a-1) corresponds to a range of pixels (7″) containing the entire nebula N159-5 along the slit. The spectrum (a-2) corresponds to a range of pixels (0.″9) containing the stars #2-66, 71, 75. In this spectrum the emission and absorption lines found between 2.14 μm and 2.15 μm are artefacts. The spectrum (a-3) corresponds to a range of pixels (0.″7) containing the star #2-55.

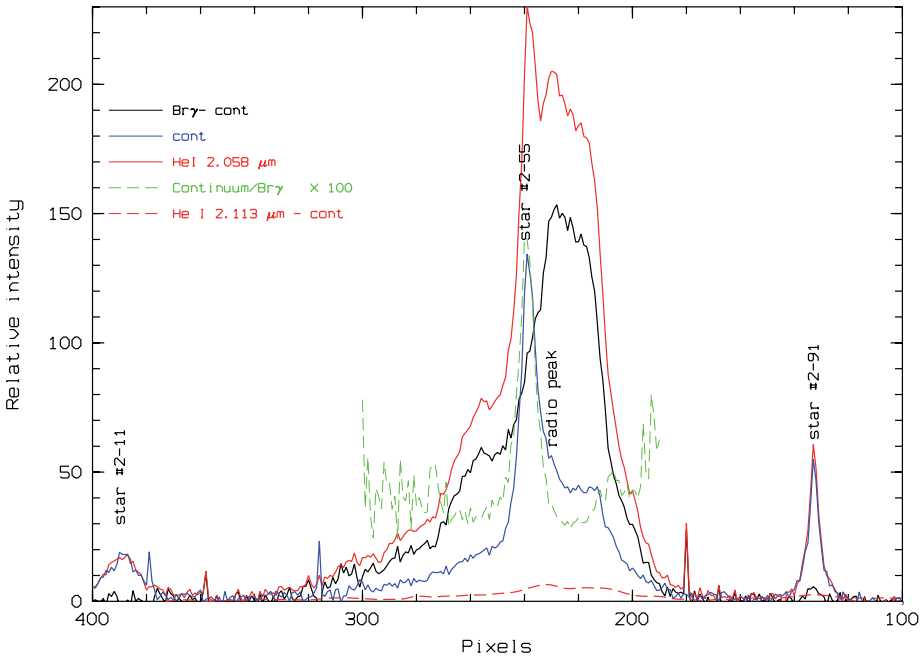

Fig. 10. Intensity distribution along the slit (a) of 17″ length (1 pixel = 0.05273″) crossing stars #2-11, #2-55 and #2-91 (Fig. 2). The solid black line represents the Brγ emission line after continuum subtraction. The corresponding nearby continuum is plotted in blue. The red line represents the intensity distribution of the He I 2.058 μm emission line. The dashed red line represents the He I 2.113 μm emission after continuum subtraction and the green one to the continuum/Brγ ratio multiplied by a factor of 100.

3.6. Radio

A comparison between the 3 cm radio image of N159-5 of Indebetouw et al. (2004) with our *K*-band image shows that most of the radio continuum emission is associated with the western wing (Fig. 5). We locate the radio peak towards star #2-57, coinciding with the western part of (b). Our position of the radio peak compared with their Fig. 16b is shifted ≈0.″4 to the south. Figure 10 shows that the maximum emission of the Brγ line as well as the HeI 2.11 μm line is superposed on the position of the radio source. This is characteristic of an HII region. The strong radio emission superposing the NIR emission in the western wing and the presence of several stars at this location, as in SH2 269, strengthens the idea that N159-5 is not ionized by #2-55 alone.

3.7. H_2 emission

We have detected molecular H_2 emission mainly between stars #2-11 and #2-91 (Fig. 10). This is primarily emission from the

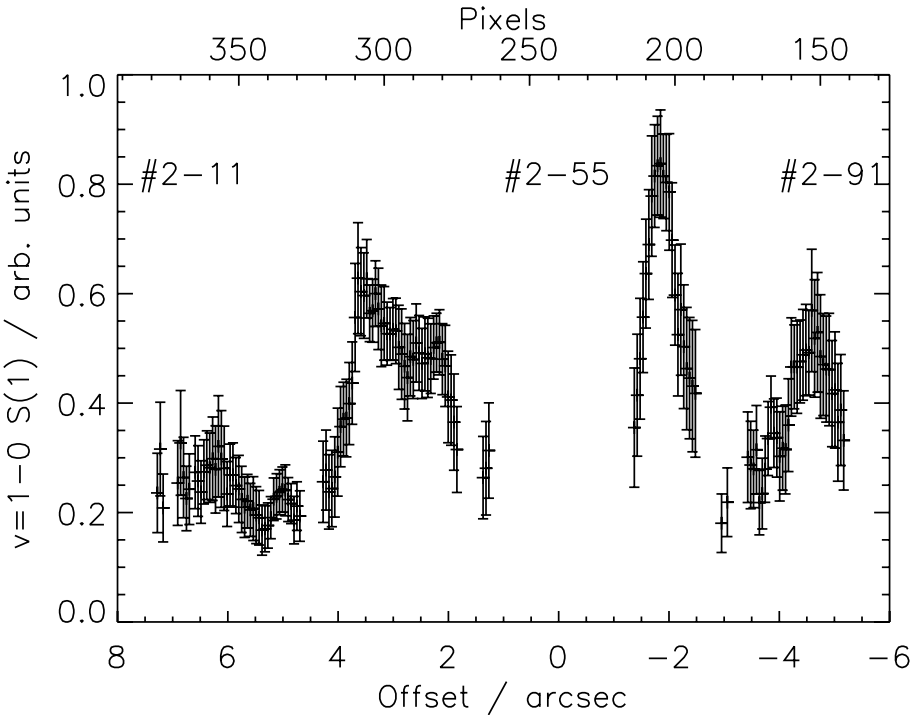

Fig. 11. The H_2 v = 1−0 S(1) profile along the slit. Coordinates are given with respect to star #2-55. The original spectrum has been smoothed by a factor of 11, but only in the spatial direction. The positions of stars #2-11, #2-55 and #2-91 are marked.

Table 6. Integrated H_2 emission over the four regions, 11NW, 55SE, 55NW and 91SE identified in Fig. 11 and in the text. Each brightness is given with respect to v = 1−0 S(1).

Line	λ (μm)	11NW	55SE	55NW	91SE
v = 1−0 S(1)	2.121	1.00	1.00	1.00	1.00
v = 1−0 S(0)	2.223	0.87 ± 0.35	0.86 ± 0.26	0.82 ± 0.32	–
v = 2−1 S(1)	2.247	–	0.98 ± 0.29[a]	0.55 ± 0.47	0.64 ± 0.27

[a] The line profile is significantly broader than other line profiles, and this value should only be taken as an upper limit.

strong v = 1−0 S(1) line. The emission allows us to identify 4 regions of high H_2 brightness: north-west of star #2-11 (11NW; 4″–2.″2), south-east (2.″2–0.5″) and north-west (−0.″5–−1.″4) of star #2-55 (55SE and NW) and south-east of star #2-91 (91SE; −1.″4–−3″). In Fig. 11 we show the v = 1−0 S(1) emission along the slit (a). We have smoothed the image in the spatial direction by applying a boxcar of width 11 pixels degrading the spatial resolution to ∼0.″35. The width of each region is ∼0.4–1.2 pc. These intensity variations are also present in Fig. 1c of Krabbe et al. (1991) who imaged N159-5 in the H_2 v = 1−0 S(1) line using subarcsec spatial resolution. We spatially integrate the emission over each of the regions resulting in a higher S/N ratio for the weaker H_2 lines. We have identified 3 H_2 lines in the regions, and their brightness with respect to v = 1−0 S(1) is shown in Table 6.

None of these lines suffer from atmospheric absorption, considering a $V_{\rm lsr}$ of 235 km s^{-1} (Johansson et al. 1998), as it can be derived from the solar spectrum atlas (Livingston & Wallace 1991) with the help of a handy piece of home-made software[1]. The lines may suffer from differential reddening (Mathis 1990). If we assume the reddening law derived by Mathis (1990) where $(\lambda_1/\lambda_2)^{-\alpha}$ is the relative extinction in magnitudes and α is estimated to be ∼1.7 and if we assume a K-band extinction of 1mag at the wavelength of the v = 1−0 S(1) transition (2.121 μm) then the v = 2−1 S(1) line may be overestimated by 10%. The K-band extinction is poorly known for this region, and we have chosen to ignore effects of differential reddening here.

In the following we will briefly go through what can be learned from the observed line emissions in terms of shock- and photodissociation region (PDR)-excitation. For PDRs we will be using the "Meudon PDR code" (Le Petit et al. 2006) and for shock models we will be using the one described in Flower & Pineau des Forêts (2003).

The excitation mechanism is very likely a PDR and not shocks for the following reasons. The width of each region is several tenths of a pc, indicating that if the excitation mechanism was a shock, then it would have to be a magnetic C-type shock rather than a non-magnetic J-type shock. However to create widths of the order of 1 pc it is necessary to have either a high magnetic field or low preshock density. In shock models the magnetic field is usually assumed to be frozen into the pre-shock gas at a flux density of $b \times [n_{\rm H}({\rm cm}^{-3})]^{1/2}$ μGauss. If a C-type shock were to be responsible for the observed width, b would have to be greater than 10 or $n_{\rm H}$ less than 10^3 cm^{-3}. This would however produce low values of the relative brightness of v = 2−1 S(1) (<0.2; Kristensen et al. 2007, in preparation). The relative v = 1−0 S(0) brightness predicted by the models would be lower than 0.3. Neither of these is reconcilable with

[1] http://www.u-cergy.fr/LERMA-LAMAP/informatique/raiesH2/index.html

observations. We cannot rule out that there may be a contribution from shocks in the region, but, at our spatial resolution it is not possible to resolve individual shock features (see Sect. 3.8).

The relative brightness of $v = 2-1$ S(1) has classically been used to discriminate between shocks and PDRs. Here we find that the relative brightness is ∼0.6 which is readily reproduced by PDR models (Le Petit et al. 2006). The main obstacle to fitting the observed brightness with PDR models is the high relative brightness of the para line $v = 1-0$ S(0). This could be explained by a value of the ortho/para ratio lower than the high temperature equilibrium value of 3. Low ortho/para ratios are not uncommon in PDRs and have been observed previously (e.g. Chrysostomou et al. 1993; Habart et al. 2003).

Using the relative brightness of $v = 2-1$ S(1) it is possible to estimate the density using the "Meudon PDR Model" (Le Petit et al. 2006). We find that the best-fit models have a density less than a few times 10^5 cm^{-3} independently of the incident radiation field. Without further observational constraints it is not possible to limit the density further. This may be compared with the density found in for example N88, another HEB in the SMC. Here it was found from observations of several rovibrational H_2 lines that the density is $\sim 10^3$ cm^{-3} (Testor et al. 2005). We cannot rule out that the density in N159-5 is different from 10^3 cm^{-3}.

3.8. Proposed morphology of the N159-5 region

We propose the following model of the N159-5 region. Overall, the structure is comparable to M42 (O'Dell 2001), where young OB stars (the Trapezium cluster) form at the edge of the molecular cloud. The massive stars irradiate the parent molecular cloud, creating the "veil" or "lid" of ionized material in front of the molecular cloud. The surface of the underlying molecular cloud will be lit up by the massive stars and a blister of ionized gas will be created. The stars that are currently forming inside the molecular cloud are all deeply embedded and only observable in the mid-infrared or at longer wavelengths (Beuther et al. 2004). In the Orion nebula this is observed in a face-on geometry. Observations of the N159-5 region show that in Hα the nebula is symmetric with two bright lobes of emission (hence the name of the nebula: the Papillon Nebula; Heydari-Malayeri et al. 1999). However, *K*-band images show only the Western lobe. In this western lobe a deeply embedded cluster has been observed at sub-mm wavelengths (Indebetouw et al. 2004). We therefore propose that the N159-5 region is in many aspects similar to the Orion Nebula with at least two differences: i) we are seeing the nebula in an edge-on geometry, compared to Orion; and ii) for such a distant object we do not have enough spatial resolution to distinguish emissions characteristic of knots associated to shocks as it is likely swamped by the dominant PDR emission. In this scenario the eastern lobe of Hα emission (no infrared counterpart) would correspond to the Orion lid, and the western lobe is the molecular cloud itself corresponding to the location of the 3 cm radio contours in Fig. 5. This also matches our spectroscopic data in which the slit passes through the central exciting source of the nebula at a position angle of 130.3°. The brightest part of the PDR is seen just north-west of star #2-55, while the PDR south-east of star #2-55 is more elongated and not as bright. This would be true if the PDR to the south-east is less dense than that to the north-west, given that they are both exposed to the same radiation field.

4. Conclusion

We present high spatial resolution imaging of $FWHM \sim 0\farcs12-0\farcs25$ in the *K*-band of the HEB N159-5 and its immediate environment, and the main results are as follows:

- N159-5 is associated with a cluster that contains at least 38 stars centered approximatively on the bright central star #2-55 and not visible at optical wavelengths. Owing to the high extinction of N159-5, most of these stars could be classified as OB type.
- The bright western wing of N159-5 contains an embedded stellar concentration associated with the 3 cm radio peak. The continuum emission surrounding star #2-55, particularly on its western side, is found to be relatively strong.
- The star #2-55 is classified of type O8 V. This classification and the high spatial resolution of the present observations enable us to conclude that star #2-55 could be a single star.
- N159-5 is ionized not only by the O8 V star #2-55, but also by other low- to high-mass stars.
- The H_2 infrared emission covers almost the entire length of the slit. We show that the excitation mechanism is caused predominantly by PDRs and not by shocks.

We also show that the morphology and structure of N159-5 are comparable with galactic regions such as SH2 269 and Orion.

New imaging data using higher spatial resolution provided by the NACO S13 camera in other *IR*-bands and spectroscopy are still necessary to obtain a better understanding of the very complex content of the HII region N159-5 in a region of low metallicity.

Acknowledgements. We thank the anonymous referee for his careful reading of the manuscript and comments to improve the paper. We are indebted to M. Heydari-Malayeri and R. Indebetouw for providing us HST Hα and 3 cm radio images of N159-5. We would also like to thank the Directors and Staff of the ESO-VLT for making possible these observations and particularly the NACO team for their excellent support. J.L.L., L.K. and S.D. would like to acknowledge the support of the French PCMI program "Physico Chimie du Milieu Interstellaire", funded by the CNRS. D.F. would like to acknowledge the Aarhus Centre for Atomic Physics (ACAP), funded by the Danish Basic Research Foundation. This research has made use of the Simbad database, VizieR and Aladin operated at CDS, Strasbourg, France, and the NASA's Astrophysics Data System Abstract Service.

References

Beuther, H., Zhang, Q., Greenhill, L. J., et al. 2004, ApJ, 616, L31
Bik, A., Kaper, L., Hanson, M. M., & Smits, M. 2005, A&A, 440, 121
Bollato, A., Jakson, J., Israel, F., Zhang, X., & Kim, S. 2000, ApJ, 545, 234
Brooks, K., & Whiteoak, J. 1997, MNRAS, 291, 395
Caswell, J. L., & Haynes, R. F. 1981, MNRAS, 194, 33
Churchwell, E., Walmsley, C. M., & Wood, D. O. S. 1992, A&A, 253, 541c
Cole, A. A. 1998, ApJ, 500, L137
Comeron, F., & Claes, P. 1998, A&A, 335, L13
Crysostomou, A., Brand, P. W. J. L., Burton, M. G., & Moorhouse, A. 1993, MNRAS, 265, 329
Cutri, R. M., et al. 2003, The IRSA 2MASS All-Sky Point Source Catalog, NASA/IPAC Infrared Science Archive, http://irsa.ipac.caltech.edu/applications/Gator/
Eiroa, C., & Casali, M. M. 1995, A&A, 303, 87
Flower, D. R., & Pineau des Forêts, G. 2003, MNRAS, 343, 390
Fukui, Y. 2005, IAU Symp., 227, 328
Gatley, I., Becklin, E. E., Hyland, A. R., & Jones, T. 1981, MNRAS, 197, 17
Habart, E., Boulanger, F., Verstraete, L., et al. 2003, A&A, 397, 623
Hanson, M., Luhman, K., & Rieke 2002, ApJs, 138, 35
Henize, K. G. 1956, ApJS, 2, 315
Heydari-Malayeri, M., & Testor, G. 1982, A&A, 111, L11

Heydari-Malayeri, M., & Testor, G. 1985, A&A, 144, 98
Heydari-Malayeri, M., Testor, G., Baudry, A., Lafon, G., & de la Noe, J. 1982, A&A, 113, 118
Heydari-Malayeri, M., Rosa, M. R., Charmandaris, V., Deharveng, L., & Zinnecker, H. 1999, A&A, 352, 665
Hunt, M., & Whiteoak, J. B. 1994, PASAu, 11, 68
Indebetouw, R., Johnson, K., & Conti, P. 2004, AJ, 128, 2206
Israel, F. P., & Koorneef, J. 1991, A&A, 248, 404
Israel, F. P., Maloney, P. R., Geis, N., et al. 1996, ApJ, 465, 738
Jiang, Z., Yao, Y. J., Baba, D., et al. 2003, ApJ, 596, 1064
Johansson, L., Greve, A., Booth, R., et al. 1998, A&A, 331, 857
Jones, T. J., Hyland, A. R., Straw, S., et al. 1986, MNRAS, 219, 603
Jones, T., Woodward, M., Boyer, M., Gehrz, R., & Polomski, E. 2005, ApJ, 620, 731
Krabbe, A., Storey, J., Rotaciuc, V., Drapatz, S., & Genzel, R. 1991, IAU Symp. 148, 205
Kristensen, L. E., Ravkilde, T. L., Field, D., Lemaire, J. L., & Pineau des Forêts, G. 2007, A&A, 469, 561
Kristensen, L. E., Pineau des Forêts, G., Lemaire, J. L., & Field, D., in preparation
Livingston, W., & Wallace, L. 1991, NSO Technical Report, Tucson: National Solar Observatory, National Optical Astronomy Observatory
Lejeune, T., & Shaerer, D. 2001, A&A, 366, 538
Le Petit, F., Nehmé, C., Le Bourlot, J., & Roueff, E. 2006, ApJS, 164, 506
Martin-Hernandez, Vermej, R., & van der Hulst, J. M. 2005, A&A, 433, 205
Mathis, J. 1990, ARA&A, 28, 37
Meynadier, F., Heydari-Malayeri, M., Deharveng, L., et al. 2004, A&A, 422, 119
Nakajima, Y., Kato., D., Nagata, T., et al. 2005, AJ, 129, 776
O'Dell, C. R. 2001, ARA&A, 39, 99
Rantakyrö, F. T., Rubio, M., Johansson, L. E. B., Chini, R., & Merkel-Ferreira, E. 2005, ASP Conf. Ser., 344, ed. C. Lidman, & D. Alloin
Rieke, G., & Lebofsky, M. 1985, ApJ, 288, 618
Scalise, E., & Braz, M. A. 1981, Nature, 290, 36
Sharpless, S. 1959, ApJS, 4, 257
Smith, L. J., Noriss, R. P. F., & Crowther, P. A. 2002, MNRAS, 337, 1309
Stetson, P. B. 1987, PASP, 99, 191
Storm, J., Carney, B. W., Gieren, W. P., et al. 2004, A&A, 415, 531
Testor, G. 2001, A&A, 372, 667
Testor, G., Lemaire, J. L., Field, D., & Callejo, G. 2005, A&A, 497, 506
Walborn, N., & Parker, J. 1992, ApJ, 399, 87

Online Material

Table 3. a) K photometry of Field 1 outside Field 2.

Id.	α (2000)	δ (2000)	X	Y	K	Error	Id.^{mey}	K^{mey}
1-9	5 40 4.34	−69 45 4.50	503.05	7.49	16.68	0.04	370	16.67
1-8	5 40 5.77	−69 45 4.48	362.29	8.32	15.52	0.02	417	15.43
1-10	5 40 5.56	−69 45 4.12	383.05	14.88	17.02	0.05		
1-11	5 40 5.86	−69 45 3.96	353.03	18.27	15.35	0.01	421	15.39
1-12	5 40 5.31	−69 45 3.74	407.23	22.30	18.14	0.13		
1-13	5 40 6.14	−69 45 3.49	325.36	26.67	16.18	0.03	436	16.00
1-14	5 40 4.20	−69 45 3.32	516.77	29.94	16.67	0.03		
1-15	5 40 5.67	−69 45 3.02	371.31	35.74	17.92	0.10		
1-16	5 40 4.11	−69 45 2.77	525.96	40.62	16.24	0.04	364	16.30
1-17	5 40 5.14	−69 45 2.72	423.94	41.20	15.99	0.04		
1-18	5 40 4.59	−69 45 2.66	478.12	42.25	17.70	0.09		
1-19	5 40 3.87	−69 45 2.03	549.51	54.60	17.84	0.10		
1-20^{d}	5 40 4.89	−69 45 1.73	448.81	60.38	17.09	0.04		
1-21	5 40 5.50	−69 45 2.53	390.76	50.36	18.02	0.06		
1-22	5 40 6.44	−69 45 1.57	296.44	63.14	13.43	0.01	444	13.34
1-24	5 40 4.94	−69 45 1.54	443.14	63.87	17.75	0.07		
1-23	5 40 5.38	−69 45 1.48	400.06	64.75	17.56	0.08		
1-25	5 40 8.86	−69 45 1.46	57.13	65.62	16.84	0.04	506	16.80
1-26	5 40 5.30	−69 45 1.24	408.20	69.68	17.58	0.06		
1-27	5 40 5.62	−69 45 1.15	376.19	71.22	13.22	0.00	410	13.02
1-28	5 40 2.22	−69 45 0.80	711.37	77.89	15.72	0.05	303	15.68
1-29	5 40 6.00	−69 45 0.66	338.96	80.63	17.39	0.05		
1-30	5 40 5.88	−69 45 0.60	351.56	81.48	15.83	0.02	422	15.58
1-31	5 40 1.63	−69 45 0.36	769.80	86.47	16.65	0.04	285	16.78
1-32	5 40 7.86	−69 45 0.33	156.04	86.65	16.21	0.04	484	16.18
1-33	5 40 0.90	−69 45 0.19	841.64	89.38	15.04	0.01	263	14.88
1-34	5 40 5.48	−69 45 0.08	390.76	91.54	16.51	0.03		
1-35	5 40 3.77	−69 45 0.05	559.10	92.11	17.04	0.05	351	17.21
1-36	5 40 4.67	−69 44 59.92	470.56	94.53	16.43	0.05	381	16.48
1-37	5 40 6.35	−69 44 59.45	305.09	103.48	18.48	0.15		
1-38	5 40 2.78	−69 44 58.82	656.97	115.63	16.81	0.03	317.1^{m}	16.32
1-39	5 40 2.80	−69 44 58.43	654.82	122.63	16.74	0.04	317.1^{m}	16.32
1-41	5 40 0.78	−69 44 58.21	853.17	126.75	16.83	0.04		
1-40	5 40 1.30	−69 44 58.21	801.83	127.09	16.18	0.04	278	16.24
1-42	5 40 4.13	−69 44 57.83	523.85	134.14	13.93	0.01	365	13.86
1-43	5 40 2.16	−69 44 57.72	717.77	136.48	17.61	0.06		
1-44	5 40 1.22	−69 44 57.67	810.52	137.06	16.25	0.04	275	16.34
1-45	5 40 5.87	−69 44 57.36	351.67	143.06	18.19	0.16	423	18.62
1-46	5 40 6.72	−69 44 57.23	268.15	145.37	18.42	0.15	453	18.90
1-47	5 40 1.03	−69 44 56.70	828.83	155.39	17.97	0.14		
1-48	5 40 7.99	−69 44 56.51	142.86	159.22	17.98	0.10		
1-49	5 40 2.01	−69 44 56.40	731.78	161.03	18.09	0.11		
1-50	5 40 0.80	−69 44 55.91	850.96	170.41	17.50	0.07	259	17.73
1-52	5 40 1.95	−69 44 55.22	738.12	183.53	17.64	0.07	295	17.62
1-53	5 40 8.11	−69 44 55.11	131.32	185.59	16.66	0.06	493	16.70
1-54	5 40 5.06	−69 44 54.95	431.59	188.66	17.27	0.06	395	17.75
1-56	5 40 7.12	−69 44 54.81	229.27	191.69	17.25	0.07	469	17.49
1-57	5 40 2.58	−69 44 54.70	676.48	193.78	17.44	0.06	315	17.75
1-58	5 40 8.99	−69 44 54.67	44.80	194.19	17.95	0.10		
1-59	5 40 8.64	−69 44 54.15	79.46	203.90	17.44	0.07	500	17.66
1-60	5 40 3.65	−69 44 54.09	571.22	204.94	16.42	0.06	346	16.59
1-62	5 40 7.33	−69 44 53.27	208.40	220.41	17.88	0.08	471	17.99
1-61	5 40 9.33	−69 44 53.27	11.52	220.82	16.87	0.04	517^{m}	17.78
1-64	5 40 2.33	−69 44 51.65	701.31	251.48	17.35	0.06		
1-65	5 40 0.30	−69 44 51.38	900.83	256.64	17.17	0.05	242	17.36
1-66	5 40 5.70	−69 44 50.91	368.51	265.69	18.31	0.13	414	18.44
1-67	5 40 8.59	−69 44 50.74	84.68	268.35	13.00	0.01	499	12.90

Table 3. a) continued.

Id.	α (2000)	δ (2000)	X	Y	K	Error	Id.^{mey}	K^{mey}
1-68	5 40 4.67	−69 44 50.69	470.02	269.71	17.82	0.09	383	18.29
1-69	5 40 1.63	−69 44 50.55	769.28	272.23	17.33	0.05	284	17.44
1-70	5 40 3.35	−69 44 50.25	600.15	277.78	17.02	0.05	334	17.41
1-71	5 40 2.25	−69 44 50.00	708.74	282.76	18.11	0.12		
1-72	5 40 1.49	−69 44 49.29	783.14	296.29	16.90	0.05	281	17.15
1-73	5 40 3.67	−69 44 49.18	569.11	298.10	15.06	0.01	348	15.31
1-74	5 40 4.69	−69 44 49.12	467.86	299.35	18.16	0.15		
1-80	5 40 7.72	−69 44 46.54	169.57	348.03	18.25	0.16		
1-92	5 40 0.37	−69 44 42.48	894.36	425.41	15.72	0.01	246	15.56
1-95	5 40 1.80	−69 44 41.54	753.14	443.11	17.94	0.11	288	18.27
1-98	5 40 9.22	−69 44 41.10	22.56	451.56	15.90	0.02	512	15.81
1-111	5 40 1.58	−69 44 39.35	774.51	484.48	17.98	0.09	282	18.58
1-112	5 40 0.98	−69 44 39.26	833.85	486.52	17.79	0.08		
1-114	5 40 1.90	−69 44 38.96	743.30	491.86	16.53	0.05		
1-127	5 40 1.75	−69 44 37.73	758.44	515.34	14.49	0.01	287	14.35
1-132	5 40 4.46	−69 44 37.37	491.01	522.42	14.36	0.01	371	14.30
1-136	5 40 0.99	−69 44 36.63	832.56	536.10	15.80	0.01	267	15.65
1-143	5 40 9.16	−69 44 35.12	28.53	565.01	16.71	0.07	509	17.13
1-153	5 40 1.62	−69 44 31.52	771.11	633.10	17.57	0.08	283	17.93
1-154	5 40 0.40	−69 44 31.33	890.86	636.98	17.58	0.07	247	17.75
1-157	5 40 8.59	−69 44 30.91	84.46	644.42	17.38	0.06		
1-161	5 40 7.12	−69 44 29.95	228.64	662.84	17.04	0.05	468	17.64
1-174	5 40 7.81	−69 44 26.16	160.78	734.66	18.78	0.19		
1-177	5 40 0.33	−69 44 25.31	897.83	750.66	18.53	0.17		
1-178	5 40 0.90	−69 44 25.20	841.26	752.97	17.29	0.05	261	17.60
1-179	5 40 5.28	−69 44 23.88	409.81	777.97	16.99	0.04	399	17.28
1-180	5 40 4.99	−69 44 23.53	438.69	784.51	16.76	0.04	390	17.09
1-182	5 40 6.71	−69 44 23.03	269.54	794.17	13.33	0.01	450	13.25
1-183	5 40 2.32	−69 44 22.95	701.71	795.64	17.72	0.08	308	18.04
1-184	5 40 3.18	−69 44 22.84	616.74	797.65	17.25	0.04	327	17.61
1-185	5 40 1.06	−69 44 22.32	825.96	807.59	17.29	0.06	269	17.59
1-186	5 40 8.78	−69 44 21.71	65.10	819.20	17.18	0.08	504	17.47
1-187	5 40 6.48	−69 44 21.25	291.58	828.23	18.21	0.11		
1-188	5 40 7.72	−69 44 20.67	169.75	838.72	18.15	0.12	479	18.31
1-189	5 40 2.46	−69 44 20.20	687.90	847.53	17.63	0.09		
1-191	5 40 3.68	−69 44 19.63	567.43	858.76	16.68	0.02		

^{mey} Label and K magnitude of stars extracted from the photometry of Meynadier et al. (2004); ^{m} multiple star; ^{d} star embedded in a tight diffuse nebula.

Table 3. b) *K* photometry of Field 2.

Id.	α (2000)	δ (2000)	*X*	*Y*	*K*	Error	Id.^{mey}	K^{mey}
2-2	5 40 2.75	−69 44 46.98	855.95	7.66	18.84	0.099		
2-3	5 40 4.04	−69 44 46.93	602.61	9.85	16.90	0.026	360	16.54
2-4	5 40 3.65	−69 44 46.76	678.13	15.54	18.55	0.092		
2-5	5 40 2.58	−69 44 46.60	888.19	22.53	18.98	0.132		
2-6	5 40 3.52	−69 44 46.49	704.82	26.54	17.44	0.038	341	17.14
2-7	5 40 2.47	−69 44 46.07	910.33	42.28	14.55	0.012	313	14.61
2-8	5 40 5.39	−69 44 45.69	336.45	56.25	17.83	0.040		
2-9	5 40 5.89	−69 44 44.56	238.10	99.81	17.38	0.045	424	17.47
2-10	5 40 2.90	−69 44 44.15	826.33	114.76	19.17	0.130		
2-11	5 40 5.38	−69 44 43.82	338.23	127.74	13.16	0.003	404	12.91
2-12	5 40 6.81	−69 44 43.11	55.87	154.21	16.17	0.021	459	16.21
2-13	5 40 3.52	−69 44 42.72	703.38	168.78	17.94	0.060	340	17.70
2-14	5 40 3.30	−69 44 42.64	747.69	172.72	18.98	0.144		
2-15	5 40 2.40	−69 44 41.76	925.12	206.08	17.78	0.042		
2-16	5 40 4.48	−69 44 41.35	514.78	221.53	18.81	0.112		
2-17	5 40 2.69	−69 44 41.30	867.75	223.49	19.02	0.123		
2-18	5 40 4.26	−69 44 41.13	558.88	229.97	19.20	0.141		
2-19	5 40 6.12	−69 44 41.08	190.99	232.09	17.31	0.040	434	17.34
2-21	5 40 4.00	−69 44 41.02	609.75	233.57	19.45	0.169		
2-20	5 40 4.92	−69 44 41.02	428.18	233.64	18.57	0.075		
2-22	5 40 5.47	−69 44 40.72	319.85	244.76	16.94	0.027	407	16.84
2-23	5 40 6.99	−69 44 40.44	20.13	255.35	18.86	0.103	467	18.43
2-24	5 40 6.76	−69 44 40.28	65.67	262.09	18.42	0.072	455	17.98
2-25	5 40 4.38	−69 44 40.09	534.41	269.45	18.21	0.063		
2-26	5 40 4.84	−69 44 39.87	444.57	277.20	18.52	0.089		
2-27	5 40 5.00	−69 44 39.84	412.49	278.77	19.27	0.174		
2-28	5 40 4.72	−69 44 39.73	468.20	282.82	18.93	0.120		
2-29	5 40 4.16	−69 44 39.48	577.88	292.47	18.95	0.117		
2-30	5 40 4.47	−69 44 39.37	515.97	295.83	17.79	0.044		
2-31	5 40 2.64	−69 44 39.07	877.72	307.44	18.09	0.051		
2-32	5 40 4.33	−69 44 39.02	545.21	309.51	18.13	0.058		
2-33	5 40 4.48	−69 44 38.91	514.60	313.45	17.50	0.037		
2-34	5 40 4.60	−69 44 38.85	490.54	315.51	18.52	0.082		
2-35	5 40 4.51	−69 44 38.85	508.30	316.30	16.74	0.026		
2-36	5 40 4.23	−69 44 38.80	563.66	317.67	17.50	0.033		
2-38	5 40 2.84	−69 44 38.77	838.48	319.57	17.27	0.027	318^{m}	16.75
2-37	5 40 4.36	−69 44 38.74	537.85	319.73	19.28	0.159		
2-39	5 40 2.79	−69 44 38.63	846.86	324.07	18.00	0.048	318^{m}	
2-40	5 40 4.72	−69 44 38.58	467.80	326.42	18.08	0.053		
2-41	5 40 4.52	−69 44 38.49	507.91	329.85	18.52	0.089		
2-42^{d}	5 40 6.80	−69 44 38.44	57.92	331.70	18.21	0.071	457	17.03
2-43	5 40 6.00	−69 44 38.44	215.60	332.02	17.73	0.041	428	17.71
2-44	5 40 4.43	−69 44 38.38	524.90	333.25	17.89	0.053		
2-46	5 40 2.57	−69 44 38.38	890.73	333.70	18.45	0.068		
2-45	5 40 4.32	−69 44 38.36	546.77	334.40	17.57	0.052		
2-47	5 40 3.92	−69 44 38.22	625.99	340.41	16.95	0.031		
2-48	5 40 4.58	−69 44 38.14	495.93	343.44	18.96	0.115		
2-49	5 40 3.42	−69 44 38.11	723.27	343.87	18.76	0.099		
2-50	5 40 4.62	−69 44 37.92	486.49	351.20	19.97	0.315		
2-51	5 40 4.29	−69 44 37.81	552.80	355.49	16.78	0.033		
2-53	5 40 4.14	−69 44 37.62	582.42	362.52	16.85	0.034		
2-52	5 40 4.76	−69 44 37.62	460.71	362.90	17.86	0.049		
2-54	5 40 5.45	−69 44 37.56	323.87	365.26	18.41	0.101	405	18.19
2-55	5 40 4.45	−69 44 37.42	519.94	370.12	14.33	0.019	371^{m}	14.30
2-57	5 40 4.33	−69 44 37.40	544.87	370.94	16.55	0.021		
2-56	5 40 4.47	−69 44 37.37	517.00	372.03	15.25	0.126	371^{m}	
2-60	5 40 4.19	−69 44 37.37	571.47	372.56	17.06	0.040		

Table 3. b) continued.

Id.	α (2000)	δ (2000)	X	Y	K	Error	Id.^{mey}	K^{mey}
2-58	5 40 4.25	−69 44 37.31	560.99	374.24	17.38	0.046		
2-59	5 40 4.62	−69 44 37.34	487.64	373.49	17.32	0.040		
2-61	5 40 4.26	−69 44 37.23	558.03	377.75	17.48	0.049		
2-62	5 40 4.37	−69 44 37.18	537.21	379.52	16.82	0.022		
2-63	5 40 4.32	−69 44 37.07	547.09	384.08	17.14	0.034		
2-64	5 40 4.50	−69 44 36.98	510.58	386.98	16.67	0.024		
2-65	5 40 4.99	−69 44 36.96	414.14	387.56	18.63	0.078		
2-66	5 40 4.36	−69 44 37.07	537.57	383.23	17.32	0.058		
2-67	5 40 4.45	−69 44 36.93	520.55	388.93	17.81	0.049		
2-68	5 40 6.30	−69 44 36.82	156.32	392.76	18.22	0.061		
2-69	5 40 4.52	−69 44 36.68	506.41	398.34	17.84	0.046		
2-70	5 40 4.41	−69 44 36.60	528.82	401.86	17.44	0.051		
2-71	5 40 4.33	−69 44 36.54	543.70	403.70	17.20	0.031		
2-72	5 40 2.24	−69 44 36.46	955.71	406.36	18.06	0.058		
2-73	5 40 4.44	−69 44 36.46	522.91	407.05	17.22	0.029		
2-74	5 40 5.12	−69 44 36.35	388.60	410.58	19.38	0.170		
2-75	5 40 4.28	−69 44 36.32	553.54	411.50	16.19	0.013		
2-76	5 40 4.44	−69 44 36.19	522.74	417.21	17.05	0.027		
2-77	5 40 4.24	−69 44 36.16	563.06	417.75	17.07	0.027		
2-79	5 40 3.76	−69 44 35.91	656.08	427.18	17.09	0.030	350	17.15
2-78	5 40 4.98	−69 44 35.91	415.93	427.35	18.38	0.073		
2-80	5 40 3.35	−69 44 35.83	736.97	430.09	17.70	0.044		
2-81	5 40 5.03	−69 44 35.75	406.08	433.21	19.24	0.170		
2-82	5 40 5.13	−69 44 35.75	386.58	433.95	19.40	0.173		
2-83	5 40 5.94	−69 44 35.39	227.39	447.01	15.66	0.020	427	15.73
2-84	5 40 5.27	−69 44 35.31	360.15	450.56	19.36	0.155		
2-85	5 40 4.73	−69 44 35.17	466.38	455.81	17.90	0.048		
2-86	5 40 3.42	−69 44 34.90	723.07	465.49	18.59	0.085	335	17.76
2-87	5 40 5.16	−69 44 34.68	381.08	474.12	16.86	0.038		
2-88	5 40 4.87	−69 44 34.35	438.76	487.33	18.32	0.064		
2-89	5 40 6.34	−69 44 34.24	148.37	490.51	16.51	0.031		
2-90	5 40 4.11	−69 44 34.13	587.31	495.06	19.05	0.131		
2-91	5 40 3.80	−69 44 33.00	648.88	537.92	15.52	0.020	353	15.52
2-92	5 40 4.00	−69 44 32.62	610.05	552.46	19.33	0.154		
2-93	5 40 3.01	−69 44 32.48	803.61	557.72	18.08	0.073	322	18.28
2-94	5 40 4.93	−69 44 32.09	425.61	571.95	19.16	0.153		
2-95	5 40 5.15	−69 44 31.85	382.72	582.06	19.06	0.148		
2-96	5 40 5.02	−69 44 31.77	407.77	584.43	19.14	0.132		
2-97	5 40 4.34	−69 44 31.27	542.09	603.70	19.24	0.157		
2-98	5 40 5.16	−69 44 31.08	380.87	610.42	17.95	0.064		
2-99	5 40 5.08	−69 44 30.91	396.82	616.64	18.97	0.134		
2-100	5 40 5.42	−69 44 30.42	329.15	635.85	17.71	0.052		
2-101	5 40 5.09	−69 44 30.34	394.11	638.82	18.06	0.052		
2-102	5 40 6.06	−69 44 29.49	203.28	670.77	16.58	0.034	432	16.68
2-103	5 40 3.21	−69 44 29.13	764.43	684.60	18.47	0.065	330	18.31
2-104	5 40 5.67	−69 44 29.10	281.02	685.46	16.09	0.038	412	16.12
2-105	5 40 5.79	−69 44 29.05	256.15	687.38	19.18	0.121		
2-106	5 40 6.54	−69 44 28.96	108.32	691.07	18.96	0.125		
2-107	5 40 5.08	−69 44 28.88	396.17	694.11	19.03	0.142		
2-108	5 40 6.67	−69 44 28.22	84.53	719.58	19.57	0.191		
2-109	5 40 2.51	−69 44 27.18	903.58	758.58	18.68	0.090		
2-110	5 40 4.68	−69 44 27.10	475.10	762.18	17.34	0.040	382	17.42
2-111	5 40 3.25	−69 44 26.46	756.92	785.80	17.71	0.038	331	17.56
2-112	5 40 6.47	−69 44 25.75	123.97	812.39	19.38	0.181		
2-113	5 40 5.63	−69 44 25.67	288.30	815.53	17.62	0.048		
2-114	5 40 5.20	−69 44 25.50	373.67	822.60	19.22	0.187		
2-116	5 40 5.83	−69 44 25.39	249.71	826.75	15.67	0.029	418	15.67

^{mey} Label and K magnitude of stars extracted from the photometry of Meynadier et al. (2004); ^{m} multiple star; ^{d} star embedded in a tight diffuse nebula.